The Stacking Faulted Nature of the Narrow Gap Semiconductor $Sc_2Si_2Te_6$

Florian Pielnhofer,*[a, b] Sebastian Bette,*[a] Roland Eger,[a] Viola Duppel,[a] Jürgen Nuss,[a] Christian Dolle,[c] Robert E. Dinnebier,[a] and Bettina V. Lotsch*[a, d]

Dedicated to Prof. Wolfgang Schnick on the occasion of his 65th birthday

Crystals of $Sc_2Si_2Te_6$ have been grown and its crystal, micro- and electronic structures were investigated. The layered character of the title compound exhibits stacking faults that impede a full structural characterization by single crystal X-ray diffraction due to diffuse scattering. Based on high resolution transmission electron micrographs and diffraction patterns, the stacking faulted nature of the real structure of $Sc_2Si_2Te_6$ has been revealed. Different stacking models were derived from the idealized, faultless structure and the stacking disorder was quantitatively analyzed by Rietveld refinement of powder X-ray diffraction patterns. An energetic comparison of the stacking models by density functional theory is in line with the experimental observations. Further, the bonding situation was investigated by electronic structure calculations. $Sc_2Si_2Te_6$ is a narrow gap semiconductor with an indirect band gap of 0.65 eV.

Introduction

The research on layered chalcogenides has experienced an immense upturn in the past few years. Especially the transition metal dichalcogenides MQ_2 (M=Ti, Zr, Hf, V, Nb, Ta, Mo, W, Tc, Re, Pd, Pt; Q=S, Se, Te) are of recent interest due to their large variety of different (opto)electronic and transport properties.[1–4] Future applications might benefit from the fact that these materials can be exfoliated into 2D sheets while preserving some of their bulk properties.[5,6] Quantum confinement effects lead to additional characteristics. The transition metal in these compounds usually exhibits a trigonal prismatic or (distorted) octahedral coordination sphere. The lamellar hexachalcogeno-hypodisilicates and -germanates with the general composition $A_2T_2Q_6$ (A=Al, In, Sb, Bi, Sc, V, Cr; T=Si, Ge; Q=Se, Te) represent a related class of materials. The atoms A and dimers of T are coordinated by the Q atoms and form layers with an overall honeycomb motif.

Similar isotypic 2D layers are also known from $M^{(+II)}P(S/Se)_3$ or $M^{(+II)}_2P_2(S/Se)_6$ compounds (M=transition or main group metal).[7] Honeycomb like arrangements in materials such as graphene or many ternary transition metal oxides gather intriguing quantum effects[8] that make these hexagonal pattern motifs extremely popular in solid state and materials science. These compounds, however, were observed to be notoriously stacking faulted,[9] which seriously impeded their structural characterization.[10–12]

Only ten members of the $A_2T_2Q_6$ family have been reported so far: $Sc_2Si_2Te_6$,[13] $V_2Si_2Se_6$,[14] $Cr_2Si_2Se_6$,[14] $Cr_2Si_2Te_6$,[15,16] $Cr_2Ge_2Te_6$,[17] $Al_2Si_2Te_6$,[13] $In_2Si_2Te_6$,[18] $In_2Ge_2Te_6$,[19] $Sb_2Si_2Te_6$[20,21] and $Bi_2Si_2Te_6$.[19] A structural characterization of $Cr_2Si_2Se_6$, $Sc_2Si_2Te_6$ and $V_2Si_2Se_6$ is still missing, only lattice parameters as obtained from X-ray powder diffraction (XRPD) are available in the literature. The Cr-compounds were intensely studied due to their magnetic properties.[17,22,23] Recent investigations on few layer-crystals have shown that nanosheets of $Cr_2Si_2Te_6$ and $Cr_2Ge_2Te_6$ are very rare examples of two-dimensional materials exhibiting a ferromagnetic ground state.[24] Further studies on $Cr_2Ge_2Te_6$ examine its potential as a thermoelectric material.[25] Increasing thermopower is achieved by A site substitution with Mn.[26] 2D slabs of the transition metal containing $M_2T_2Q_6$ (M=V, Cr, Mn, Fe, Co, Ni) family haven been modeled and their magnetic properties have been studied by density functional theory (DFT), indicating the general interest in this class of materials.[27]

In, Sb and Bi based $A_2T_2Q_6$ compounds are narrow gap semiconductors ($E_G < 0.5$ eV) and $Sb_2Si_2Te_6$ and $Bi_2Si_2Te_6$ exhibit

[a] Dr. F. Pielnhofer, Dr. S. Bette, R. Eger, V. Duppel, Dr. J. Nuss, Prof. Dr. R. E. Dinnebier, Prof. Dr. B. V. Lotsch
Max Planck Institute for Solid State Research
Heisenbergstr. 1, 70569 Stuttgart, Germany
E-mail: s.bette@fkf.mpg.de
b.lotsch@fkf.mpg.de
[b] Dr. F. Pielnhofer
New address: Institute of Inorganic Chemistry, University of Regensburg, 93053 Regensburg, Germany
E-mail: florian.pielnhofer@ur.de
[c] Dr. C. Dolle
Laboratory for Electron Microscopy, Microscopy of Nanoscale Structures and Mechanisms, Karlsruhe Institute of Technology, Engesserstr. 7, 76131 Karlsruhe, Germany
[d] Prof. Dr. B. V. Lotsch
Department of Chemistry, Ludwig-Maximilians-Universität München, Butenandtstr. 5–13, 81377 München, Germany

significantly better thermoelectric performance than $Cr_2Ge_2Te_6$.[20,21] $Sb_2Si_2Te_6$ reaches ZT values up to 1.08, which is increased to even 1.6 when turning it into a cellular nanostructured network with Si_2Te_3.[21a] The lattice thermal conductivity of $Bi_2Si_2Te_6$ is even lower than that of $Sb_2Si_2Te_6$ and its power factors can be enhanced by increasing the hole concentration which is achieved by Pb doping.[21b] The moderate thermopower in $In_2Si_2Te_6$ can be also tuned by increasing the carrier concentration and as a consequence, decreasing the electrical resistivity and Seebeck coefficients whereas the resulting figure of merit ZT increases. This is achieved by Si versus P substitution up to 10%.[28] $In_2Ge_2Te_6$ was synthesized and structurally characterized for the first time in 2009 by Seidlmayer[19] and subsequently "rediscovered" in 2017.[29] In this study stacking fault disorder is claimed to be responsible for the low thermal conductivity. The stacking faults in $In_2Ge_2Te_6$ are coherently scattering domains as revealed by transmission electron microscopy (TEM) and XRPD. Four different stacking models were used for a multiphase LeBail-fit to explain their nature. While almost all members of the $A_2T_2Q_6$ family of compounds crystallize in space group $R\bar{3}$ (no. 148) with an ABC stacking of the layers, $Al_2Si_2Te_6$ and $In_2Si_2Te_6$ crystallize in space group $P\bar{3}$ (no. 147) with an eclipsed AA stacking of the honeycomb layers. Polytypism in $A_2T_2Q_6$ compounds has not been observed yet. However, deeper insights into the microstructure only exist for $In_2Ge_2Te_6$ so far.

Simultaneously to $Al_2Si_2Te_6$, $Sc_2Si_2Te_6$, which is isoelectronic to the Al and In compounds, was reported in the same work but a structural characterization was missing.[13] Although indexed powder diffraction data and lattice parameters were given, possible isotypism to $Cr_2Si_2Te_6$ was not discussed.

In this study we focus on the determination of the ideal and real structure of $Sc_2Si_2Te_6$ including a detailed analysis on the types and amounts of stacking fault disorder by single crystal and X-ray powder diffraction as well as high resolution transmission electron microscopy (HRTEM). The energetics of the stacking faults were further examined by quantum chemical modelling of hypothetical polytypes, supporting the experimental findings. In addition, we present the electronic structure of $Sc_2Si_2Te_6$ in real and reciprocal space and show that it exhibits a narrow band gap.

## Results and Discussion

Single crystal X-ray diffraction

The title compound forms air and moisture sensitive flaky crystals (up to 300 μm lateral size) with a golden greenish metallic gloss (Figure 1a). The platelet-like morphology of the crystals is further emphasized by scanning electron microscopy (SEM) images (Figure 1c). The 2:2:6 (1:1:3) stoichiometry is confirmed via energy dispersive X-ray (EDX) spectroscopy (see Table S6 and Figure S2). $Sc_2Si_2Te_6$ comprises neutral layers separated by van der Waals gaps. Diffuse rods in the diffraction patterns along the c^* axis (Figure 1b) indicate stacking fault
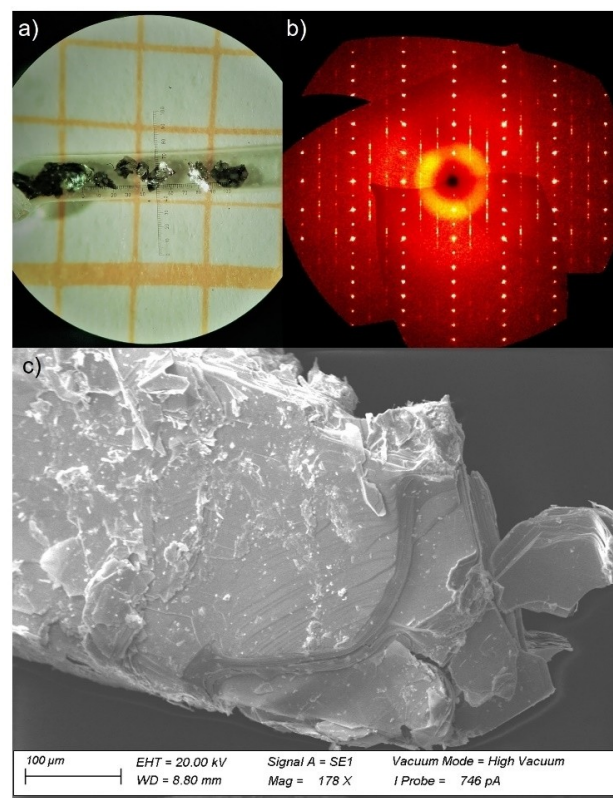
Figure 1. a) Crystals of $Sc_2Si_2Te_6$ (on underlying millimeter paper); b) view of the reciprocal 1kl plane: Diffuse scattering of the reflections along the c^* axis; c) SEM micrograph showing the platelet-like morphology of the crystals.

disorder within the crystals. As a consequence, the single crystal structure analysis led to insufficient results.

An initial refinement of the single crystal data assuming isotypicity to $Fe_2P_2Se_6$ with a staggered ABC stacking sequence (space group $R\bar{3}$) lead to a disordered structure model with only one of the two Sc positions fully occupied (Sc1; 3b; Figure 2 b). The second scandium atom (Sc2; 6c) is located at the center of gravity of a Si–Si dumbbell. The two Si positions of the dumbbell and the Sc position in the same octahedral coordination sphere are occupationally disorderd with site occupancy factors (SOF) of 0.5 for each atom. Further, a smaller and even more disordered structure can be derived from the diffraction patterns (see Supporting Information, Table S5). In this smaller cell (space group $P\bar{3}m1$) with lattice parameters of $a = 4.0409(2)$ Å and $c = 7.0863(4)$ Å a full disorder of Sc atoms (SOF = 0.67; 1a) and Si–Si (SOF = 0.33; 2c) dumbbells is found (Figure 2 a). While the parameter c in the small cell is one third of the lattice parameter of the $R\bar{3}$ cell with ABC stacking, the a parameter corresponds to the Sc–Sc distances in the honeycomb (Figure 2 c, d). Thus, the stacking sequence of the small trigonal cell corresponds to an eclipsed AA type stacking. However, both structure models obtained via single crystal X-ray diffraction appear reasonable due to the well-known phenomenon of stacking fault disorder in such types of compounds and a more detailed analysis via TEM and XRPD is
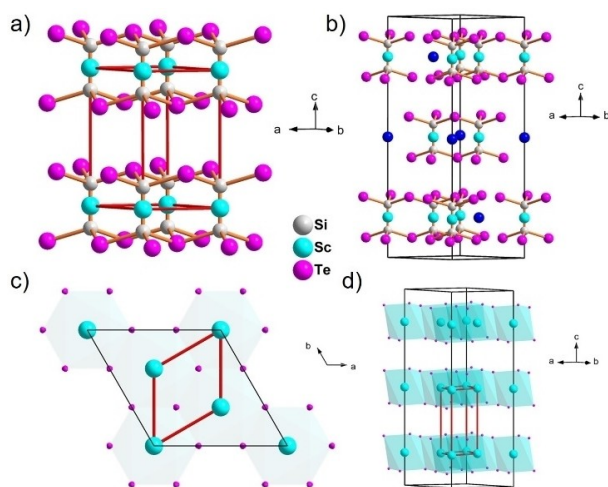
Figure 2. a) Small, occupationally Sc—Si disordered unit cell in $P\bar{3}m1$; b) large unit cell in $R\bar{3}$ with partially ordered Sc-sites (dark blue atoms represent fully occupied Sc positions); c), d) relation of the disordered unit cells, only Sc and Te atoms are shown (small cell: red edges, large cell: black edges).

Figure 3. a) SAED, PED and simulated diffraction patterns for $Sc_2Si_2Te_6$ on the basis of the **S1** stacking type and alternating **S1** + **S3** stacking, zone axes specified in the figure; b) HRTEM micrograph with marked stacking vectors **S1**, **S2** and **S3**, zone axis [100].

crucial. It should also be noted that stacking fault disorder is often compensated in crystal structure refinements by introducing an artificial occupational disorder of the cation sites within the honeycomb layers.[10,11] Therefore, the occupational disorder within the layers most likely results from stacking fault disorder that cannot be compensated in a trivial way during the structural refinement against single crystal data.

Transmission electron microscopy

The stacking fault disorder in the real structure of $Sc_2Si_2Te_6$ is obvious from X-ray and electron diffraction patterns. The diffuse rods in zone axis pattern [100] which are aligned parallel to c^* are also visible in the precession electron diffraction (PED) and selected area electron diffraction (SAED) patterns (see Figure 3 a). The simulated pattern of the faultless structure (sim. **S1**; ABC stacking, **S1** stacking vectors only) only consists of sharp reflections. Further comparison of simulated **S1** and experimental PED patterns of zone axis [001] reveals additional sharp reflections in the experimental pattern.

Indeed, these additional spots originate from the intersection of the diffuse rods and the Ewald sphere, hinting towards intrinsic faults. We further included a structure model with alternating **S1** and **S3** vectors (AB stacking) to the comparison of experimental and simulated patterns. This sequence (**S1** + **S3**) acts as a simple model of an infinite domain including periodic stacking faults. The additional reflections in zone axis [001] are also visible in the simulated pattern of **S1** + **S3**, which makes this rather ordinary model an additional plausible scenario, although it consists of homogeneous stacking only.

HRTEM micrographs (zone axis [100]) perfectly visualize the three different possibilities of stacking (see Figure 3 b). The staggered stacking of the layers is highlighted by **S1** and **S3**
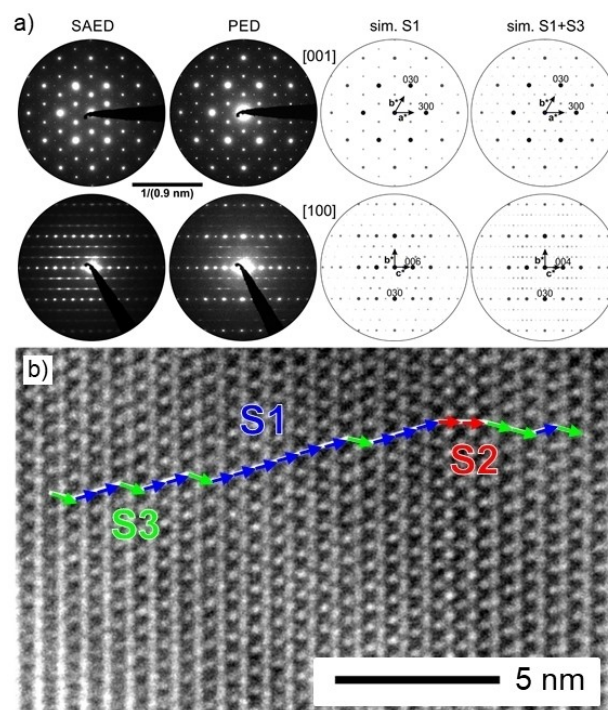
vectors that mainly occur in $Sc_2Si_2Te_6$. **S1** and **S3** are the main stackings as obtained for at least four different crystallites. Interestingly, not only the staggered stacking is present; to a very small amount we also find an eclipsed stacking of the honeycomb layers as indicated by the **S2** vector. **S2** stacking is the common stacking motif in $In_2Si_2Te_6$ and $Al_2Si_2Te_6$ (space group $P\bar{3}$). A more detailed explanation of the stacking vectors **S1** (staggered), **S2** (eclipsed) and **S3** (staggered) is given below (Figure 7, Figure 8).

Description of the idealized crystal structure

$Sc_2Si_2Te_6$ crystallizes in the $Fe_2P_2Se_6$-type structure in space group $R\bar{3}$ (no. 148) with Wyckoff sequence fc^2 and Pearson-code $hR10$. It exhibits a layered anion sub-lattice that is isotypic to the iodide sublattice of CdI_2, with Te-layers stacked perpendicular to the c-axis in an $\alpha\beta\alpha\beta$ fashion (Figure 4 c). Layers of octahedral and tetrahedral voids are apparent in this sub-lattice that are arranged in an alternating fashion. As only the octahedral voids are occupied by Si—Si dimers and Sc ions (Figure 4 a), $Sc_2Si_2Te_6$ can be considered as a layered compound with tetrahedral interlayer voids. Within a layer each $Si_2Te_{6/3}$ octahedron is surrounded by 6 $ScTe_{6/3}$ octahedra, resulting in a *honeycomb*-like motif (Figure 4 b). Due to the stacking order, the anion sublattice can also be described by a primitive $1/3$-c-subcell. The overall rhombohedral lattice symmetry, however, is
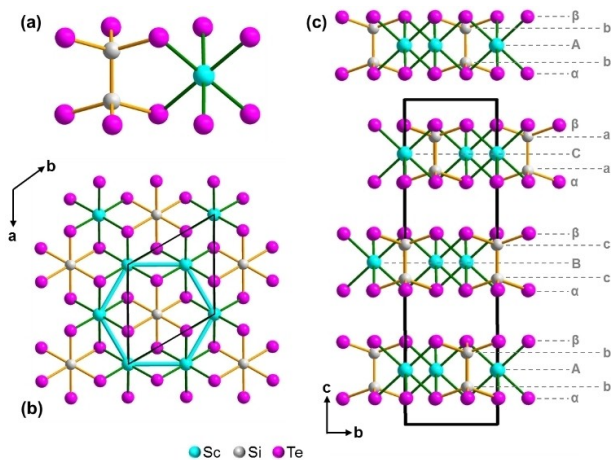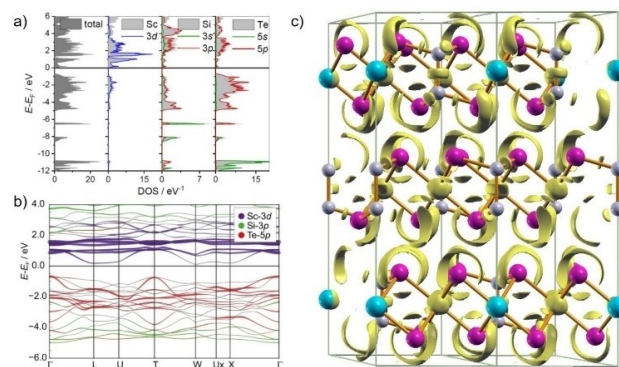
Figure 4. (a) Coordination spheres of Si and Sc in the crystal structure of $Sc_2Si_2Te_6$, (b) packing diagram in *c*-direction, the Sc_6-honeycomb motif in the cation sublattice is highlighted by turquoise bonds, (c) stacking order of the Sc- (capital Latin letters), Si- (small Latin letters) and Te-layers (small Greek letters).

Figure 5. a) Atomic site and orbital projected density of states, b) electronic band structure of $Sc_2Si_2Te_6$ with orbital contributions projected onto the bands (size of the dots corresponds to amount of orbital contribution) and c) electron localization function (ELF = 0.8 shown in yellow; Si: grey, Sc: blue, Te: pink).

governed by the ABC stacking order of Sc and by the aabbcc stacking order of Si (Figure 4 c).

The anionic $Si_2Te_6^{6-}$ unit is isostructural to the ethane molecule in a staggered conformation. The center of gravity of the homoatomic Si_2 dumbbells is located at a center of inversion resulting in two sets of 2×3 identical atomic distances d(Si–Te) = 2.477(3) Å. The Si–Si distance is 2.246(9) Å, which is slightly shorter than other Si–Si single bonds in related compounds (2.324 Å in $Cr_2Si_2Te_6$[16] and 2.300 Å in $In_2Si_2Te_6$[18]). Due to a slight asymmetric distortion of the octahedra, there are also two sets of 2×3 identical Sc–Te distances d(Sc–Te) = 2.958(3) Å and 2.969(2) Å. These distances are very similar compared to two modifications of Sc_2Te_3 (d_{Sc-Te} = 2.88 Å to 2.95 Å).[30,31] The distortion of the octahedra is less pronounced than in $Cr_2Si_2Te_6$ (d(Cr–Te) = 2.763(1) Å and 2.81(0) Å) and $Al_2Si_2Te_6$ (d(Al–Te) = 2.865(13) and 2.951(12) Å). The van der Waals gap between the layers is 3.38 Å.

Electronic structure

Scalar-relativistic electronic structure calculations have been performed to gain insights into the bonding situation and to investigate the electronic structure of the idealized crystal structure with **S1** stacking vectors only. $Sc_2Si_2Te_6$ is an indirect band gap semiconductor with the valence band maximum located at the Γ point and the conduction band minimum at the W point of the first Brillouin zone. Although the PBE functional tends to underestimate band gaps, the title compound can still be classified as narrow gap semiconductor with a calculated value of 0.65 eV. Fat band plots (see Figure 5 b) visualize the composition of the bands in the vicinity of the Fermi level and highlight the Te-5*p* orbitals being responsible for the valence band maximum as well as Sc-3*d* and Si-3*p* for

the conduction band minimum. Slightly populated Sc-3*d* states in the range of −1 to −5 eV represent bonding to Te-5*p* within the distorted octahedra. Si–Si and Si–Te bonding interactions are represented by the DOS maxima at −8 eV, −6.5 eV and between −4 and −5 eV. The lone pair character of the Te-5 *s* is represented by sharp DOS maxima below −10 eV (see Figure 5 a). In addition to bonding analysis in reciprocal space we also carried out real space bonding analysis by calculating the electron localization function (ELF). Covalent Si–Si bonds, as expected for Si(III) in the ethane like unit, are represented by ELF attractors at values of 0.8 (see Figure 5 c). The 3D ELF plots further highlight the Te lone pairs, which occupy space in the van der Waals gap.

Evaluation of the crystal structure refinement

The graphical result of the Rietveld refinement of the crystal structure of $Sc_2Si_2Te_6$ is presented in Figure 6. By quick inspection the fit seems to be quite good and the agreement factors are also acceptable (R-wp = 5.91%, G.O.F. = 1.57). A closer inspection, however, reveals systematic deviation of the calculated pattern (red line) from the measured ones (blue circles). Some reflection intensities, e.g. 006 and 119, were underestimated, whereas other reflection intensities e.g. 113, 030, were overestimated. This could be an effect of slight preferred orientation effects due to insufficient grinding. In addition, the difference Fourier map revealed residual electron density in the center of gravity of the Si–Si bond and above and below the Sc site. Another indicator for an incomplete structure model was found during the inspection of the refined thermal displacement parameters (B_{eq}-values). The thermal displacement parameter for Te was refined to a reasonable value of 0.93 Å^2, while for Sc a slightly higher value can be expected and the Rietveld refinement resulted in a B_{eq} 1.42 Å^2. For Si, however, a thermal displacement parameter of 4.99 Å^2 was obtained, which is far too high. With respect to the
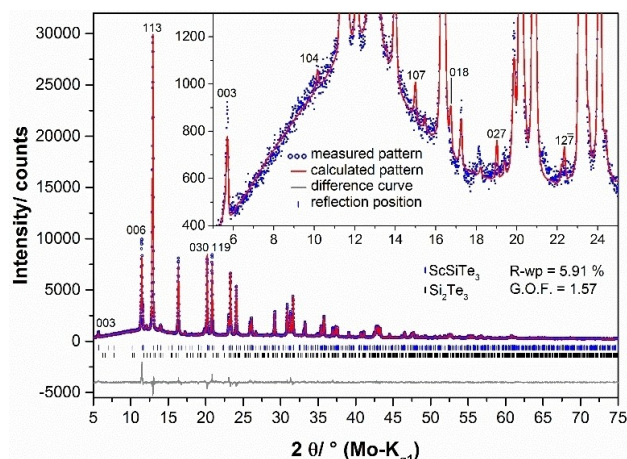
**Figure 6.** Graphical result of the final Rietveld refinement of Sc₂Si₂Te₆ at ambient conditions including selected reflection indices, low intensity reflections in the 2 θ range of (5–25)° are highlighted to illustrate systematic misfits of the diffraction pattern.

Figure 7. Derivation of possible stacking vectors in the crystal structure of Sc₂Si₂Te₆ from the positions of octahedral voids in the anion sublattice.

observed residual electron densities in the proximities of the Si and Sc sites, a Si–Sc occupational disorder was introduced into the refinement, yielding an approx. 10% occupational disorder for both sites. The agreement factors and the fit, however, were only insignificantly improved and for Sc and especially for Si unreasonable B_{eq} values were still obtained. A very close inspection of the graphical result of the final Rietveld refinement (Figure 6, inset) revealed further problems: some reflections that should have measurable intensity (104, 107, 018, 027, 1$\overline{2}$7) according to the considered structural model are not apparent. This cannot be explained by preferred orientation or any extinction rules; accordingly, no additional translational symmetry elements are present. A reasonable explanation for the observed diffraction effects is the presence of planar defects in the form of *stacking faults*, as:

1. stacking fault disorder is a common phenomenon in layered compound with honeycomb motifs;[9b,32]
2. stacking fault disorder mimics an occupational disorder in the honeycomb layers;[10b,11]
3. distinct reflections can completely vanish by the occurrence of heavy disorder.[11,33]

Derivation of a faulting model from the idealized structure

Possible stacking faults in Sc₂Si₂Te₆ can be directly derived from the crystal structure. As the anion lattice shows a close packing with tetrahedral interlayer voids, there is no alternative way of stacking. Hence possible stacking faults must originate from a shift in the stacking order of the cation lattice, exclusively. The stacking of the cation sublattice is directed by the positions of the octahedral intralayer voids. By taking an arbitrary void in layer *i* seven possible stacking vectors can be derived for the cation positions. Due to the lattice symmetry only 3 of the seven stacking vectors are symmetry independent (Figure 7). As
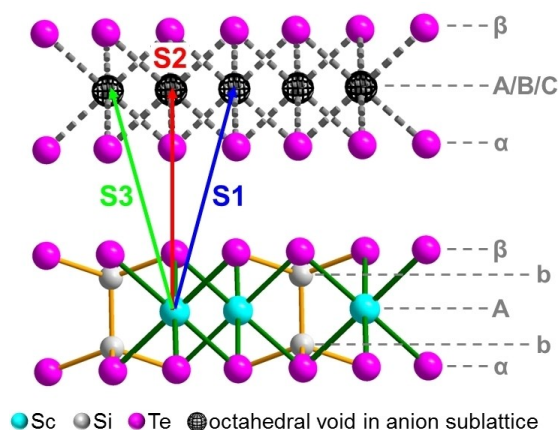
the interlayer distance is not affected by faulting, the *z*-component of each possible stacking vector is $1/3$. Taking the A-site of the Sc-sublattice as the starting point of the stacking vector, stacking in the pattern of the idealized structure would cause a shift in the cation sublattice to the B-site in layer *i+1*. Accordingly, the *x*-component of the stacking vector that should be denoted as "**S1**" is $1/3$ and the *y*-component $2/3$. This leads to a staggered stacking of the Sc₆ honeycombs (Figure 8). Alternatively the subsequent layer can be stacked without any shifts in the cation positions, i.e. an A-site is followed by another A-site (Figure 7). In consequence both the *x*- and *y*-component of stacking vector "**S2**" are 0, which leads to an eclipsed stacking (Figure 8). The cation sublattice can also exhibit a reverse stacking order, i.e. an A-site is followed by a C-site (Figure 7). This leads to a stacking vectors "**S3**" with $2/3$ as *x*- and $1/3$ as *y*-component. As **S1**-stacking, the vector **S3** leads to a staggered layer confirmation. The change from **S1**- to **S3**-stacking can also be described as twinning.
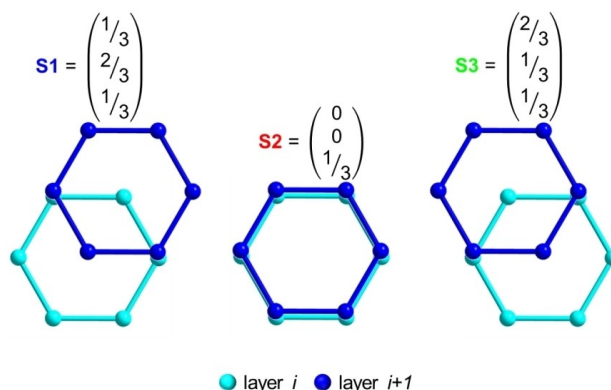

Figure 8. Illustration of the effect of the possible stacking vectors on the stacking order of the Sc₆-honeycombs.

Systematic DIFFaX studies

DIFFaX[34] simulations were employed to visualize the diffraction effects of different faulting models and to evaluate them by a comparison to the measured XRPD pattern. In order to ensure the visibility of low intensity reflections all patterns are plotted as 2θ angle vs. square root intensity.

At first a series of simulations was performed with faultless stacking of the considered stacking orders, i.e. pure **S1**-, **S2**- and **S3**-stacking (Figure 9). As Te is the strongest scatterer in $Sc_2Si_2Te_6$ and as the stacking of the anion sublattice is identical in each of the considered stacking types, the position and the intensity of the strong reflections (Figure 9, blue indices) is identical for all basic stacking types. The simulated patterns only differ in the position and intensities of the low-intensity reflections (black indices), which completely vanish in the measured pattern. As the **S2**-stacking does not exhibit
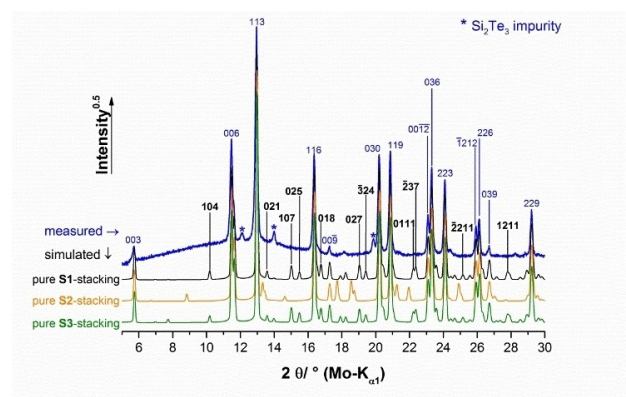
rhombohedral symmetry and therefore can be described by a $\frac{1}{3}$ c unit cell, the pattern of the low intensity reflections completely differs compared to the **S1**- and **S3**-stacking. The simulated patterns of pure **S1**- and **S3**-stacking are almost identical as both stacking orders can be described by the same rhombohedral unit cell with the same space group. Slight differences can be observed in the reflection intensities (supporting information, Figure S1). As the measured pattern almost does not exhibit any of the low intensity reflections, it can be concluded that none of the considered stacking orders is predominant or occurs in homogeneously stacked coherently scattering domains of significant size. Hence, the microstructure of the $Sc_2Si_2Te_6$ sample most likely contains many shifts among two or all of the considered stacking orders.

In order to examine the diffraction effects of stacking faults in the crystal structure of $Sc_2Si_2Te_6$ systematic simulations using three fault models were performed. In the first model random transitions between **S1**-, **S2** and **S3**-stacking were considered, whereas the second model only contains random transitions between **S1**- and **S3**-stacking, i.e. random twinning. For the sake of completeness, the crystallographic intergrowth of random **S1**−**S3**-twinning with sections showing **S1**- and **S3**-stacking in alternating fashion was considered as third faulting model. The transition probability matrices used for the simulations are presented in Table 1. In order to simplify the simulations, reasonable constraints were applied to the elements of the matrices.

Random transitions among **S1**-, **S2**- and **S3**-stacking were simulated by introducing a global fault probability, x (Table 1, upper part). As all octahedral voids in the cation sublattice are identical, transitions from **S1**-stacking to **S2**-stacking should have the same probability as transitions to **S3**-stacking. During the simulations, the fault probability was gradually increased (Figure 10 a). Even a small fault probability of 20% leads to vast broadening of the weak-intensity reflections (black indices). The high-intensity reflections are not affected by faulting, as

Figure 9. Comparison of the measured XRPD pattern of $Sc_2Si_2Te_6$ with simulated patterns from faultless stackings of the considered stacking vectors (Figure 7, Figure 8), including selected reflection indices.

Table 1. Transition probability matrices applied for the simulation of different faulting models. Variable parameters are highlighted by red font colour.

Model 1: random transitions between S1, S2 and S3

from↓	to→	S1-stacking	S2-stacking	S3-stacking
S1-stacking		1-x	x/2	x/2
S2-stacking		1-x	x/2	x/2
S3-stacking		1-x	x/2	x/2

Model 2: random twinning

from↓	to→	S1-stacking		S3-stacking	
S1-stacking		1-y		y	
S3-stacking		1-y		y	

Model 3: random twinning with intergrown domains

from↓	to→	S1-stacking	S3-stacking	S1−S3 domain S1-part	S3-part
S1-stacking		0.5-z	0.5-z	z	z
S2-stacking		0.5-z	0.5-z	z	z
S1−**S3** domain	**S1**-part	0.5·(1-ext)	0.5·(1-ext)	0	ext
	S3-part	0.5·(1-ext)	0.5·(1-ext)	ext	0
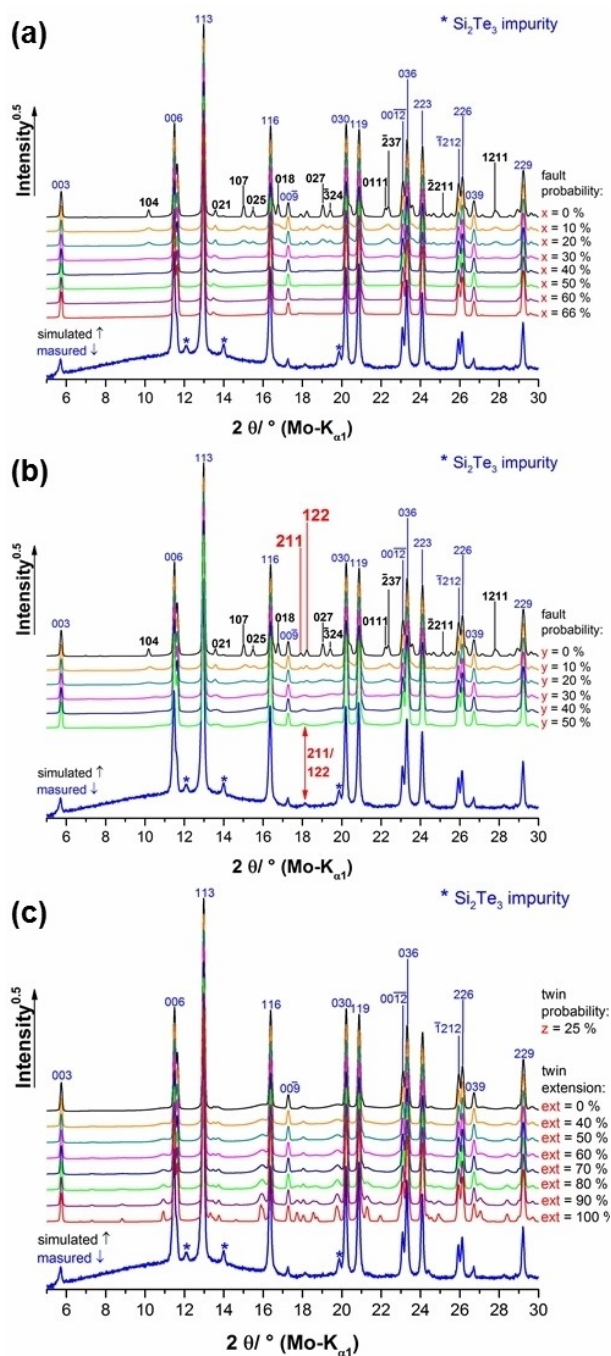
Figure 10. Systematic *DIFFaX*-simulations using 3 faulting models: (a) random transitions among **S1**-, **S2**- and **S3**-stacking (Figure 7, Figure 8), (b) random twinning, i.e. using **S1**- and **S3**-stacking exclusively and (c) random twinning with intergrown domains that exhibit **S1**−**S3** stacking in alternating fashion.

transitions among **S1**-, **S2**- and **S3**-stacking do not cause changes in the stacking of the anion sublattice. The greatest agreement between measured (blue line) and simulated pattern is achieved with a fault probability of 66%, which corresponds to a complete random distribution of the stacking vectors, i.e. the maximum degree of faulting. In this case almost all weak-

intensity reflections completely disappear, only a small remnant of the 021 reflection is still visible.

For the second faulting model that includes only transitions among **S1**- and **S3**-stacking, similar constraints in the form of a global fault probability, y (Table 1, middle part), were applied. As in the first model, even a small fault probability leads to vast broadening of the weak-intensity reflections and the highest agreement between simulated and measured pattern is achieved by the maximum degree of faulting, i.e. y = 50% (Figure 10 b). Almost all weak reflections completely vanish, and again only broad remnants of the 021 reflection and a merged 211/122 reflection are visible.

The maximum degree of random **S1**−**S3** faulting was used as the starting point for the simulations of an intergrowth with **S1**−**S3** alternating stacked domains. A fault probability, z, of 25% was applied to simulate a complete statistical occurrence of **S1**−**S3** domains (Table 1, bottom part). The extension of the **S1**−**S3** stacked domain is described by the parameter ext, which was gradually increased during the simulations (Figure 10 c). By increasing the extension of the **S1**−**S3** domains additional weak-intensity reflections appear that grow in intensity and sharpness with growing extension of the coherently scattering domains. The greatest agreement between simulated and measured pattern is achieved by a very small extension of the **S1**−**S3** domains (ext = 40%, i.e. on average there extension of the **S1**−**S3** domains within a stack of hundreds of layers is four layers or smaller).

The third faulting model can be quickly evaluated as unsuitable, as no additional weak reflections are visible in the measured pattern. As the highest agreement between measurement and simulations was obtained with a very small extension of the **S1**−**S3** domains, the overall distribution of the stacking vectors can be assumed as almost completely statistical. Hence this is covered by the second model. Both the faulting models containing a pure random distribution of **S1**-, **S2**- and **S3**-stacking (first model) and **S1**- and **S3**-stacking only (second model) lead to a good agreement between measured and calculated pattern. The vastly broadened remnants of the 021 reflection apparent in the simulated patterns, however, cannot be observed in the measured pattern. This could be attributed to the big amorphous hump caused by the capillary combined with noise in the data. The remnants of the merged 211/122 reflection that are apparent only in the simulated patterns of the second fault model that only includes **S1** and **S3**-stacking, which are also apparent in the measured pattern, seem to support this faulting model, but this indicator is weak. Hence both faulting models were included in the further investigation of the measured pattern by a Rietveld compatible approach.
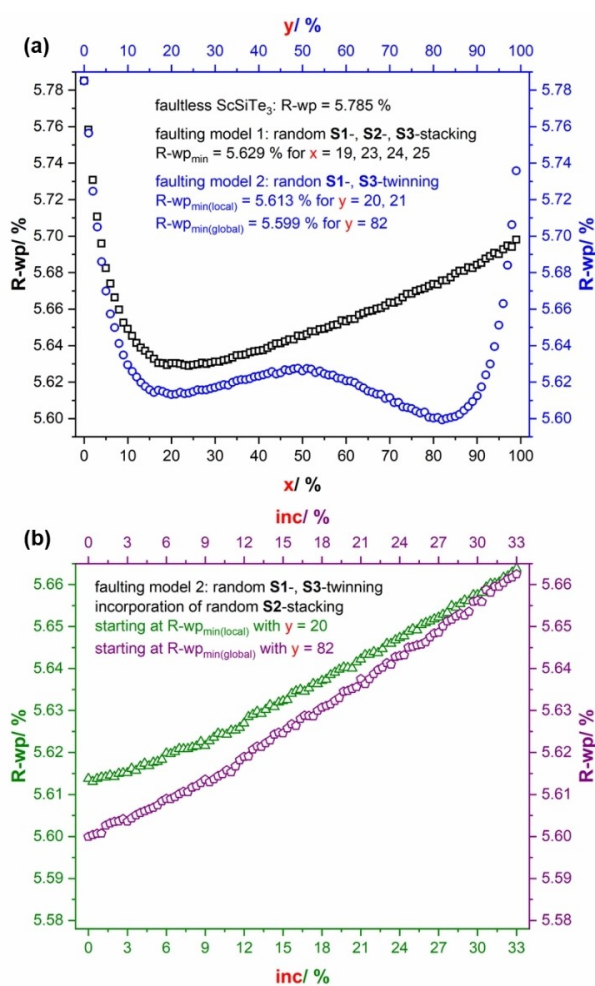
Refinement of the real structure using a Rietveld compatible approach

The diffraction pattern of $Sc_2Si_2Te_6$ was refined by using a statistical supercell approach[35,36] with 200 layers. The idealized (faultless) crystal structure was used to describe the layer constitution. All parameters, related to the constitution of the

ZAAC
Journal of Inorganic and General Chemistry
Zeitschrift für anorganische und allgemeine Chemie

RESEARCH ARTICLE

layers, i.e. atomic coordinates and lattice parameters, were kept fixed during the refinements. As a direct refinement of the transition probabilities is not possible in the statistical supercell approach, the optimizations in the parameter space of the transition probability matrices were performed as grid searches.[37,38] In total 400 Rietveld refinements were carried out.

In the first two series the faulting models that contain random transitions among **S1**-, **S2**- and **S3**-stacking (model 1) and random **S1**-, **S3**-twinning (model 2) were investigated as there is only one variable parameter in each transition probability matrix (Table 1). The results are presented in Figure 11 a as plots of the resulting R-wp value as a function of the variable parameter in the transition probability matrix.

By using the fault model 1 the resulting R-wp value drops down by increasing the fault probability x (Figure 11 a, black squares). With a fault probability of approx. (23–25) % a global minimum in the R-wp value is obtained, which is significantly lower (5.629 %) than the R-wp value (5.785 %) that results from the faultless structure. By a further increase of the fault probability, the resulting R-wp value also increases. Applying fault model 2, which only contains random **S1**-, **S3**-twinning, lower R-wp values (Figure 11 a, blue circles) can be obtained than by using fault model 1. The parameter space of fault model 2 exhibits 2 minima: a local minimum at a fault probability of (20–21) % and a global minimum at a fault probability of 82 %. This means that in contrast to the idealized structure model that contains **S1**-stacking exclusively, **S3**-stacking is predominant in the crystal structure of $Sc_2Si_2Te_6$. In addition, the **S2**-stacking pattern seems to be negligible in the microstructure of the material, as weakly indicated by the systematic *DIFFaX* studies (Table 1) and by the HRTEM images (Figure 3 b). In order to confirm this, the transition probability matrix of fault model 2 was extended by the inclusion of random transitions from and to **S2**-stacking, with a probability of **S2**-stacking as a variable parameter (Figure 11 b). Grid searches were performed with using the local (Figure 11 b, green triangles) and the global minimum (Figure 11 b, violet pentagons) of transition probability parameter space of fault model 2 as starting points. In both cases the extension of the transition probability matrix does not yield an improvement of the resulting R-wp, in contrast, an increasing probability of **S2**-stacking leads to an increase of the resulting R-wp values by ca. 0.1. At a probability for **S2**-stacking of 33 % both faulting models yield an identical R-wp, worse than the starting point. In consequence, it can be concluded that **S2**-type stacking, which leads to an eclipsed confirmation of the Sc_6-honeycomb (Figure 8, middle), is not apparent by a considerable amount in the microstructure of $Sc_2Si_2Te_6$. In this material random **S1**-, **S3**-twinning occurs without the formation of large homogeneously stacked sections that form coherently scattering domains in the crystals.

For a final Rietveld refinement the faulting model 2 with a fault probability of y = 82 % was chosen. The graphical result is displayed in Figure 11. The inclusion of stacking faults into the structural refinement enabled the proper refinement of the atomic positions. As the use of a supercell approach requires a reduction of the space group symmetry to *P*1, we introduced constraints on the atomic positions in order to mimic the layer symmetry (see Supporting Information, Figure S1). For a reliable crystal structure refinement, the inclusion of stacking faults is necessary, as even the diffraction data of the single crystals represents averaged information. This is indicated by the residual electron density between the silicon atoms (see section **Single crystal X-ray diffraction** above), which led to an unusual small Si–Si bond lengths (2.246(9) Å) during the crystal structure refinement. The structure refinement against the XRPD data, that included stacking fault disorder led to a longer Si–Si bond length of 2.464(14) Å. In addition a more reasonable isotropic thermal displacement parameter for all atoms: Te: 0.8(1) Å², Sc: 1.0(2) Å², Si: 1.6(2) Å². The final refinement also led to much better residual criteria (R-wp = 5.32, G.O.F. = 1.4) than using the structure model obtained from single crystal diffraction data (5.91 %, G.O.F. = 1.57). Finally, the calculated powder pattern does not contain any of the weak intensity reflections (Fig-

Figure 11. Plots of the R-wp vs. the transition probability from a Rietveld refinement of $Sc_2Si_2Te_6$ by using a statistical supercell approach[7] using (a) faulting model 1 and 2 (Table 1), and (b) using the global and local minimum of the parameter space of the transition probability matrix of faulting model 2 and extending it by including random transition to **S2**-stacking.

ure 12, inset) that disappear by the structural disorder. There is still a small misfit of the 006 reflection that seems to be related to slight preferred orientation effects. In order to avoid over-parametrization we did not introduce an additional correction function.
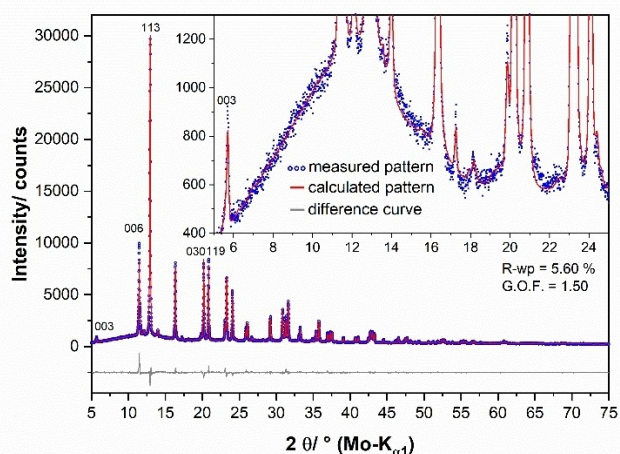
Figure 12. Graphical result of the final Rietveld refinement of the XRPD pattern of $Sc_2Si_2Te_6$ by using a statistical supercell approach[7] that contain random transitions between **S1**- and **S3**-stacking with a fault probability y = 82% (Table 1) at ambient conditions including selected reflection indices, low intensity reflections in the 2θ range of (5–25)° are highlighted to illustrate broadening of low intensity reflections due to stacking faults.
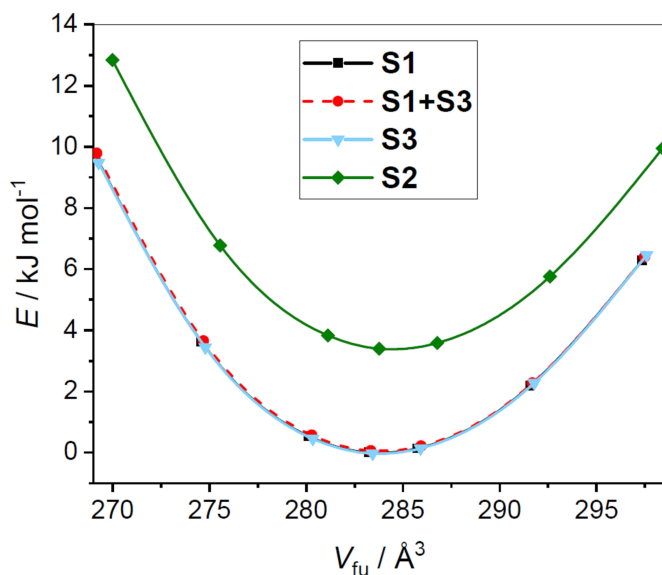
Figure 13. Calculated (DFT-PBE) E-V plots for different stacking models applied to $Sc_2Si_2Te_6$.

DFT modeling of stacking polytypes

The occurrence of stacking faults was also modelled with DFT. The layered nature of $Sc_2Si_2Te_6$ with a van der Waals gap between the layers make the inclusion of dispersion interactions a mandatory point in full structural optimizations, which was done by using the Grimme D3[39] correction. Besides the above-mentioned structure models with solely **S1**, **S2** or **S3** stacking vectors, we further constructed a hypothetical polytype with alternating **S1** and **S3** vectors, resulting in the trigonal space group $P\bar{3}$. The stacking order of the layers is ABAB and the c axis is $^2/_3$ of the idealized structure models' c axis. This model was initially also included in the *DIFFaX* simulations of the X-ray powder pattern, but led to worse fits. However, the faulting model used for the final fit allows for **S1**−**S3** transitions and therefor also small ABAB stacking domains. The energy vs volume plots of all four models (**S1**, **S1**+**S3**, **S3** and **S2**) are shown in Figure 13. The resultant lattice parameters of the minimum structures (6.95 Å) are in good agreement with the experimental value of 6.996 Å. When considering the c^* axes (corresponding to c in **S2**, $^2/_3$ c in **S1**+**S3** and $^c/_3$ in **S1** or **S3**) of the polytype models, the preferred structures' c^* value is similar (6.78 Å in all cases) while c of the **S2** model is slightly longer (6.80 Å). A comparison of the total electronic energy of the different stackings reveals that the polytypes **S1**, **S1**+**S3** and **S3** are energetically equivalent, differing only by less than 60 J mol^{-1}. This further underpins the experimental findings, namely that both **S1** and **S3** stacking co-exist in $Sc_2Si_2Te_6$. The **S2**-stacking (ABAB-type), the structural motif in $Al_2Si_2Te_6$ and $In_2Si_2Te_6$, is less stable for $Sc_2Si_2Te_6$ by 3.4 kJ mol^{-1}. This small amount of energy is also in line with our HRTEM images (Figure 3 b) that show **S2** stacking to occur in $Sc_2Si_2Te_6$ to a minimal extent.

Conclusions

The occurrence of stacking faults is a common phenomenon in layered honeycomb materials.[9b,32] In most cases like in $H_3LiIr_2O_6$[11] stacking fault disorder in the form of random layer to layer transitions affect the positions of the strongest scatteres and is therefore visible by characteristic triangular Warren-type[40] peak shapes. In other cases, e.g. in $SnTiO_3$[41] or $In_2Ge_2Te_6$[29] the microstructure consists of homogenously stacked sections with different stacking orders that lead to the different coherently scattering domains in the crystals, which appear as additional peaks in the diffraction pattern. In our current study we show that homogenous stacking in large domains is absent in $Sc_2Si_2Te_6$ and stacking fault disorder could only be discovered by subtle indicators, e.g. residual electron densities, unusual thermal displacement parameters and the absence of weak intensity reflections. From a quantum chemical point of view, the modeling of different stacking types via DFT supports the experimental findings. While the different stacking vectors that lead to staggered stacking of the Sc honeycombs are energetically equal, an eclipsed stacking is disfavored. However, the rather small difference between staggered and

eclipsed stacking also explains the occurrence of the latter in HRTEM images, although not being quantifiable by the Rietveld compatible approach. Microstructural considerations are nevertheless necessary to obtain a suitable structural model, to understand the crystal chemistry and the material's properties.

Experimental Section

Synthesis

All preparations and manipulations were done in an argon atmosphere. Crystals of $Sc_2Si_2Te_6$ were grown from a stoichiometric mixture of the elements Sc (lumps), Si (powder) and Te (powder) in vacuo-sealed quartz tubes. The tubes were heated up to 1023 K (50 K h^{-1}), held at that temperature for 10 d and cooled down to room temperature. During our synthesis attempts, it turned out that using excess Sc leads to the growth of larger crystals, since crystals of $Sc_2Si_2Te_6$ preferentially grow on the Sc pieces. The crystals have a metallic greenish golden shimmer.

Single Crystal X-ray diffraction

Single crystals suitable for single-crystal X-ray diffraction were picked under a microscope in dried petroleum and mounted into sealed glass capillaries for single-crystal X-ray diffraction measurements. Diffraction data were collected at room temperature (298 K) with a SMART-APEX-II CCD X-ray diffractometer (Bruker AXS, Karlsruhe, Germany) with graphite monochromated MoKα radiation. The reflection intensities were integrated with the SAINT subprogram in the Bruker Suite software package.[42] A multi-scan absorption correction was applied using SADABS.[43] The structure was solved by direct methods and refined by full-matrix least-squares fitting with the SHEXTL software package.[44,45]

Transmission Electron Microscopy

TEM was performed with a Philips CM30 ST (300 kV, LaB$_6$ cathode) equipped with a spinning star device enabling the use of precession electron diffraction (PED). Simulations of the diffraction patterns were obtained with the JEMS software package.[46]

SEM and EDX spectroscopy

Crystals for SEM/EDX measurements were prepared and selected in a glove box under inert gas atmosphere. Measurements were performed on a Zeiss EVO® MA15 (Carl Zeiss Microscopy Deutschland GmbH, Oberkochen) using the software SmartSEM® Version 6.05 with accelerating voltage of 20 kV. For EDS measurements a Bruker Quantax 200-Z3 Xflash630 (Bruker Corporation, Billerica, USA) was used as X-ray detector with the software Bruker Esprit 2.1.2.

Powder X-ray diffraction

Powder X-ray diffraction patterns were measured in sealed glass capillaries using a STOE StadiP diffractometer working with Ge-monochromatic MoK$_\alpha$ radiation in Debye-Scherrer geometry.

Determination of the average crystal structure

The average, i.e. idealized, faultless crystal structure of $Sc_2Si_2Te_6$ was determined using the single crystal data as starting model. The program TOPAS 6.0[47] was used for all crystal structure refinements. A Pawley fit[48] using space group $R\bar{3}$ and fits applying the fundamental parameter approach of TOPAS[49] were performed to determine the precise lattice parameters (supporting information, table S1). The background was modeled by employing Chebychev polynomials of 6th order, the hump in the background caused by the glass capillary was modeled with a broad Lorentzian shaped peak. The refinement converged quickly. Finally the crystal structure was refined by applying the Rietveld method.[50] Therefore, all profile and lattice parameters were released iteratively and atomic positions were subjected to free unconstrained refinement. Further details are presented in the Results and Discussion section. The crystallographic data have been deposited at the CDCC, deposit number: 2183862.

DIFFaX simulations

The DIFFaX routine[34] was used to model the effects of planar defects in shape of stacking faults on the diffraction pattern of $Si_2Sc_2Te_6$. All simulations were performed in recursive mode with an infinite stacking range. The peak profile was approximated by Pseudo Voigt functions that were extracted from a LeBail fit[51] of the measured diffraction pattern.

Refinement of a supercell model

For the refinement of the diffraction pattern of $Sc_2Si_2Te_6$ a supercell approach based on transition probabilities[35,36] was used. The transition probability matrices that were used for the DIFFaX simulations were also applied in this approach. In each run a random stacking sequence of 200 layers was created. For a given set of transition probabilities 100 random stacking sequences were created and the best representative (in terms of R-wp) was used. Multiple sets of transition probabilities were used in order to perform a grid search[37,38] in the parameter space of the transition probability matrix. In order to increase the calculation speed the diffraction pattern was refined in a 2 θ range from 5° to 44°.

DFT calculations

Quantum chemical calculations were performed in the framework of density functional theory (DFT) using a linear combination of Gaussian-type functions (LCGTF) scheme as implemented in CRYSTAL17.[52,53] The total energy calculations including full structural optimisations were performed with the GGA (PBE)[54] xc-functional including the Grimme D3[39] dispersion correction. The convergence criterion considering the energy was set to 1×10^{-8} a.u. with a k-mesh sampling of $12\times12\times12$. Pseudo potential basis sets for Sc and Te were taken from[55,56] and Si was described by an ell-electron basis set as taken from.[57]

The electronic structure was additionally assessed by the full potential local orbital (FPLO) method as implemented in the FPLO code (version 14.00-45).[58] Scalar-relativistic PBE calculations were carried out on a dense k-mesh of $12\times12\times12$. Experimental structure parameters were used as input.

Further, a direct space analysis of the charge density was carried out by calculating the electron localization function (ELF)[59] with TOPOND[60] interfaced to CRYSTAL. The optimized structure as obtained by the PBE-D3 method in combination with all-electron basis sets for all atoms[57,61,62] was used. In the case of Sc, an

additional *d*-polarization function (exponent: 0.1359; coefficient: 1.0) was added and for Te the outermost contraction was removed. 3D plots were visualized with XCrysDen.[63]

[1] D. Voiry, A. Mohite, M. Chhowalla, *Chem. Soc. Rev.* **2015**, *44*, 2702–2712.

[2] G. H. Han, D. L. Duong, D. H. Keum, S. J. Yun, Y. H. Lee, *Chem. Rev.* **2018**, *118*, 6297–6336.

[3] A. Kuc, T. Heine, A. Kis, *Mater. Res. Bull.* **2015**, *40*, 577–584.

[4] A. A. Testone, D. J. Lewis, P. O'Brien, *Chem. Mater.* **2016**, *28*, 1965–1974.

[5] M. Chhowalla, H. S. Shin, G. Eda, L. J. Li, K. P. Loh, H. Zhang, *Nat. Chem.* **2013**, *5*, 263–275.

[6] S. Manzeli, D. Ovchinnikov, D. Pasquier, O. V. Yazyev, A. Kis, *Nat. Rev. Mater.* **2017**, *2*, 1–15.

[7] W. Klingen, G. Eulenberger, H. Hahn, *Naturwissenschaften* **1968**, *55*, 229.

[8] K. Kitagawa, T. Takayama, Y. Matsumoto, A. Kato, R. Takano, Y. Kishimoto, S. Bette, R. Dinnebier, G. Jackeli, H. Takagi, *Nature* **2018**, *554*, 341–345.

[9] a) S. A. J. Kimber, C. D. Ling, D. J. P. Morris, A. Chemseddine, P. F. Henry, D. N. Argyriou, *J. Mater. Chem.* **2010**, *20*, 8021–8025; b) D. C. Wallace, T. M. McQueen, *Dalton Trans.* **2015**, *44*, 20344–20351.

[10] a) V. Todorova, A. Leineweber, L. Kienle, V. Duppel, M. Jansen, *J. Solid State Chem.* **2011**, *184*, 1112–1119; b) M. J. O'Malley, P. M. Woodward, H. Verweij, *J. Mater. Chem.* **2012**, *22*, 7782–7790.

[11] S. Bette, T. Takayama, K. Kitagawa, R. Takano, H. Takagi, R. E. Dinnebier, *Dalton Trans.* **2017**, *46*, 15216–15227.

[12] M. Plass, S. Bette, R. E. Dinnebier, B. V. Lotsch, *Chem. Mater.* **2022**, *34 (7)*, 3227–3235.

[13] E. Sandre, V. Carteaux, A. M. Marie, G. Ouvrard, *J. Alloys Compd.* **1994**, *204*, 145–149.

[14] J. Gopalakrishnan, K. S. Nanjundaswamy, *Mater. Res. Bull.* **1988**, *23*, 107–112.

[15] G. Ouvrard, E. Sandré, R. Brec, *J. Solid State Chem.* **1988**, *73*, 27–32.

[16] R. E. Marsh, *J. Solid State Chem.* **1988**, *77*, 190–191.

[17] V. Carteaux, D. Brunet, G. Ouvrard, G. Andre, *J. Phys. Condens. Matter* **1995**, *7*, 69.

[18] E. Sandré, V. Carteaux, G. Ouvrard, *C. R. Acad. Sci. Ser. II* **1992**, *314*, 1151.

[19] S. Seidlmayer, Dissertation, Universität Regensburg, **2009**.

[20] S. Arabbagheri, Dissertation, Universität Regensburg, **2014**.

[21] a) Y. Luo, S. Cai, S. Hao, F. Pielnhofer, I. Hadar, Z. Luo, J. Xu, C. Wolverton, V. P. Dravid, A. Pfitzner, Q. Yan, M. G. Kanatzidis, *Joule* **2020**, *4*, 159–175; b) Y. Luo, Z. Ma, S. Hao, S. Cai, Z.-Z. Luo, C. Wolverton, V. P. Dravid, J. Yang, Q. Yan, M. G. Kantzidis, *JACS* **2022**, *144*, 1445–1454.

[22] V. Carteaux, G. Ouvrard, J. C. Grenier, Y. Laligant, *J. Magn. Magn. Mater.* **1991**, *94*, 127–133.

[23] B. Siberchicot, S. Jobic, V. Carteaux, P. Gressier, G. Ouvrard, *J. Phys. Chem.* **1996**, *100*, 5863–5867.

[24] C. Gong, L. Li, Z. Li, H. Ji, A. Stern, Y. Xia, T. Cao, W. Bao, C. Wang, Y. Wang, Z. Q. Qiu, R. J. Cava, S. G. Louie, J. Xia, X. Zhang, *Nature* **2017**, *546*, 265–269.

[25] D. Yang, W. Yao, Q. Chen, K. Peng, P. Jiang, X. Lu, C. Uher, T. Yang, G. Wang, X. Zhou, *Chem. Mater.* **2016**, *28*, 1611–1615.

[26] X. Tang, D. Fan, K. Peng, D. Yang, L. Guo, X. Lu, J. Dai, G. Wang, H. Liu, X. Zhou, *Chem. Mater.* **2017**, *29*, 7401–7407.

[27] B. L. Chittari, D. Lee, N. Banerjee, A. H. MacDonald, E. Hwang, J. Jung, *Phys. Rev. B* **2020**, *101*, 085415.

[28] T. Suriwong, K. Kurosaki, S. Thongtem, *J. Alloys Compd.* **2018**, *735*, 75–80.

[29] R. Lefevre, D. Berthebaud, O. Lebedev, O. Pérez, C. Castro, S. Gascoin, D. Chateigner, F. Gascoin, *J. Mater. Chem. A* **2017**, *5*, 19406–19415.

[30] J. G. White, J. P. Dismukes, *Inorg. Chem.* **1965**, *4*, 1760–1763.

[31] A. Assoud, H. Kleinke, *Acta Crystallogr. Sect. E* **2006**, *62*, i17–i18.

[32] D. C. Wallace, C. M. Brown, T. M. McQueen, *J. Solid State Chem.* **2015**, *224*, 28–35.

[33] S. Mangelsen, B. R. Srinivasan, U. Schürmann, L. Kienle, C. Näther, W. Bensch, *Dalton Trans.* **2019**, *48*, 1184–1201.

[34] M. M. J. Treacy, J. M. Newsam, M. W. Deem, *Proc. R. Soc. London Ser. A* **1991**, *433*, 499–520.

[35] A. A. Coelho, J. S. O. Evans, J. W. Lewis, *J. Appl. Crystallogr.* **2016**, *49*, 1740–1749.

[36] C. M. Ainsworth, J. W. Lewis, C.-H. Wang, A. A. Coelho, H. E. Johnston, H. E. A. Brand, J. S. O. Evans, *Chem. Mater.* **2016**, *28*, 3184–3195.

[37] S. Bette, T. Takayama, V. Duppel, A. Poulain, H. Takagi, R. E. Dinnebier, *Dalton Trans.* **2019**, *48*, 9250–9259.

[38] S. Bette, B. Hinrichsen, D. Pfister, R. E. Dinnebier, *J. Appl. Crystallogr.* **2020**, *53*, 76–87.

[39] a) S. Grimme, J. Antony, S. Ehrlich, H. Krieg, *J. Chem. Phys.* **2010**, *132*, 154104; b) S. Grimme, S. Ehrlich, L. Goerigk, *J. Comput. Chem.* **2011**, *32*, 1456–1465; c) S. Grimme, A. Hansen, J. G. Brandenburg, C. Bannwarth, *Chem. Rev.* **2016**, *116*, 5105–5154.

[40] B. E. Warren, *Phys. Rev.* **1941**, *59*, 693–698.

[41] L. Diehl, S. Bette, F. Pielnhofer, S. Betzler, I. Moudrakovski, G. A. Ozin, R. Dinnebier, B. V. Lotsch, *Chem. Mater.* **2018**, *30*, 8932–8938.

[42] Bruker Suite, Version 2015/9. Bruker AXS Inc., Madison, WI, USA, **2015**.

[43] G. M. Sheldrick, SADABS – Bruker AXS area detector scaling and absorption correction, version 2014/5; University of Göttingen, Göttingen, Germany, **2014**.

[44] G. M. Sheldrick, *Acta Crystallogr. Sect. A: Found. Crystallogr.* **2008**, *64*, 112–122.

RESEARCH ARTICLE

[45] G. M. Sheldrick, *Acta Crystallogr., Sect. C: Struct. Chem.* **2015**, *71*, 3–8.

[46] P. A. Stadelmann, *Ultramicroscopy* **1987**, *21*, 131–145.

[47] A. A. Coelho, *J. Appl. Crystallogr.* **2018**, *51*, 210–218.

[48] G. S. Pawley, *J. Appl. Crystallogr.* **1981**, *14*, 357–361.

[49] R. W. Cheary, A. A. Coelho, J. P. Cline, *J. Res. Natl. Inst. Stand. Technol.* **2004**, *109*, 1–25.

[50] H. M. Rietveld, *J. Appl. Crystallogr.* **1969**, *2*, 65–71.

[51] A. Le Bail, H. Duroy, J. L. Fourquet, *Mater. Res. Bull.* **1988**, *23*, 447–452.

[52] R. Dovesi, A. Erba, R. Orlando, C. M. Zicovich-Wilson, B. Civalleri, L. Maschio, M. Rerat, S. Casassa, J. Baima, S. Salustro, B. Kirtman, *WIREs Comput. Mol. Sci.* **2018**, *8*, e1360.

[53] R. Dovesi, V. R. Saunders, C. Roetti, R. Orlando, C. M. Zicovich-Wilson, F. Pascale, B. Civalleri, K. Doll, N. M. Harrison, I. J. Bush, P. D'Arco, M. Llunell, M. Causà, Y. Noël, L. Maschio, A. Erba, M. Rerat, S. Casassa, CRYSTAL17 User's Manual (University of Torino, Torino, **2017**).

[54] J. P. Perdew, K. Burke, M. Ernzerhof, *Phys. Rev. Lett.* **1996**, *77*, 3865.

[55] T. Bredow, K. Jug, R. A. Evarestov, *Phys. Status Solidi B* **2006**, *243*, R10–R12.

[56] J. Heyd, J. E. Peralta, G. E. Scuseria, R. L. Martin, *J. Chem. Phys.* **2005**, *123*, 174101.

[57] F. Pascale, C. M. Zicovich-Wilson, R. Orlando, C. Roetti, P. Ugliengo, R. Dovesi, *J. Phys. Chem. B* **2005**, *109*, 6146–6152.

[58] K. Koepernik, H. Eschrig, *Phys. Rev. B* **1999**, *59*, 1743.

[59] A. D. Becke, K. E. Edgecombe, *J. Chem. Phys.* **1990**, *92*, 5397–5403.

[60] C. Gatti, S. Cassassa, Topond14 – http://www.crystal.unito.it/topond/topond.pdf, **2016**.

[61] N. M. Harrison, B. Montanari, L. Ge, **2006**, Sc_864-11G*_harrison_2006, http://www.crystal.unito.it/Basis Sets/scandium.html.

[62] http://www.tcm.phy.cam.ac.uk/~mdt26/basis sets/Te basis.txt.

[63] a) A. Kokalj, *J. Mol. Graphics Modell.* **1999**, *17*, 176–179; b) A. Kokalj, *Comput. Mater. Sci.* **2003**, *28*, 155–68.